research papers

X-ray characterization of a multichannel smart-pixel array detector

Steve Ross,[a] Michael Haji-Sheikh,[a] Andrew Huntington,[b] David Kline,[c] Adam Lee,[b] Yuelin Li,[c] Jehyuk Rhee,[b] Mary Tarpley,[d] Donald A. Walko,[c] Gregg Westberg,[a] George Williams,[b] Haifeng Zou[b] and Eric Landahl[d]*

[a]Northern Illinois University, Department of Electrical Engineering, DeKalb, IL 60115, USA, [b]Voxtel Inc., Beaverton, OR 97006, USA, [c]Advanced Photon Source, Argonne National Laboratory, Argonne, IL 60439, USA, and [d]DePaul University, Department of Physics, Chicago, IL 60614, USA. *Correspondence e-mail: elandahl@depaul.edu

The Voxtel VX-798 is a prototype X-ray pixel array detector (PAD) featuring a silicon sensor photodiode array of 48 × 48 pixels, each 130 μm × 130 μm × 520 μm thick, coupled to a CMOS readout application specific integrated circuit (ASIC). The first synchrotron X-ray characterization of this detector is presented, and its ability to selectively count individual X-rays within two independent arrival time windows, a programmable energy range, and localized to a single pixel is demonstrated. During our first trial run at Argonne National Laboratory's Advance Photon Source, the detector achieved a 60 ns gating time and 700 eV full width at half-maximum energy resolution in agreement with design parameters. Each pixel of the PAD holds two independent digital counters, and the discriminator for X-ray energy features both an upper and lower threshold to window the energy of interest discarding unwanted background. This smart-pixel technology allows energy and time resolution to be set and optimized in software. It is found that the detector linearity follows an isolated dead-time model, implying that megahertz count rates should be possible in each pixel. Measurement of the line and point spread functions showed negligible spatial blurring. When combined with the timing structure of the synchrotron storage ring, it is demonstrated that the area detector can perform both picosecond time-resolved X-ray diffraction and fluorescence spectroscopy measurements.

1. Introduction

The ideal X-ray counting detector should be able to tag each incident X-ray photon with its time of arrival, energy and angle. Furthermore, it should exhibit a large dynamic range while recording negligible dark counts. For synchrotron radiation applications, a good approximation to an ideal detector is one that can discriminate between successive X-ray bunches, can separate fluorescent from scattered X-rays, and can be scaled to an arbitrarily large number of closely spaced distinct detector array elements. The dead-time should be less that the bunch separation, and integration times of several minutes should be possible with no background. To date, there has been no detector that can meet all of these expectations. For instance, the widely adopted Pilatus detector (Henrich *et al.*, 2009) in fact has the time and energy resolution necessary for many applications, but only a single energy and timing channel is available. Therefore it is difficult to make comparative measurements: it is not possible to simultaneously record the X-rays arriving before *versus* after an event, or above *versus* below an absorption edge. Without such normalization, experiments inevitably suffer from drift and the signal-to-noise ratio ultimately is limited by the
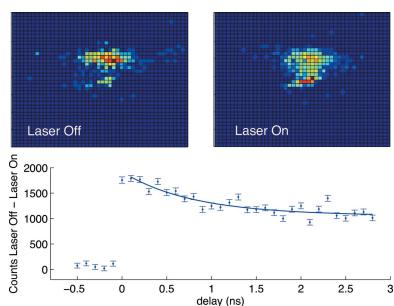
detector frame rate. It is not usually possible to optimize detectors for particular applications once they are built. Again taking the Pilatus as an example, its 90 ns timing gate is suitable for bunch discrimination at some storage rings in some operating modes such as the Advanced Photon Source (APS) in the 24-bunch (153 ns separation) standard fill pattern (Ejdrup *et al.*, 2009). However it is not possible to exchange time for energy resolution by adjusting the shaping time of each pixel amplifier in the same way that a single-element detector may be optimized. This is the central conundrum of synchrotron detector design: because detector development is such a long-term commitment it is important that the detectors that result are useful to a broad range of science and can be adapted to meet new challenges. In our 'smart pixel' approach, represented by the Voxtel VX-798 prototype presented here, two counters can be individually temporally gated, and have independent energy threshold adjustments. The multichannel pixels are combined with a scalable platform that allows the key parameters to be programmed in software (Williams *et al.*, 2013). We chose to build a pixel array detector (PAD) since they are already known to meet the necessary specifications and have a high degree of flexibility in their design (Kraft *et al.*, 2009; Rossi *et al.*, 1999; Campbell *et al.*, 1998; Vernon *et al.*, 2007; Spieler, 2005). Our detector consists of a sensor to absorb X-ray photons and convert their energy to electric signals, with the readout electronics centered around a bump-bonded application specific integrated circuit (ASIC) and a field programmable gate array (FPGA) for digital control and data acquisition systems. Our single-photon-counting PAD approach is related but complimentary to analog PADs developed for high-intensity measurements (Koerner & Gruner, 2010) where multiple photons per pixel can be recorded from a single bunch. Alternate approaches for time-gated X-ray imaging use vacuum electronics such as optical image intensifiers (Nüske *et al.*, 2010) or multichannel plates combined with GHz waveform sampling (Adams *et al.*, 2015). We first discuss the design and construction of the detector and then present its electrical and X-ray characterization including initial time-resolved and fluorescence X-ray measurements. A summary of key parameters and measured performance for the detector is given in Table 1.

2. Detector design and fabrication

2.1. Sensor

Our sensor consists of an array of silicon PIN diodes: p+, intrinsic (lightly doped n), n+ silicon. The sensor was fabricated in the Northern Illinois University Department of Electrical Engineering's Microelectronics Research and Development Laboratory (Ross *et al.*, 2013). This process begins with a 520 µm-thick Silicon Quest ⟨100⟩ 4-inch, prime, double-sided polished phosphorus-doped >10000 Ω cm float-zone wafer. We define photo masks in AutoCAD and convert to an electro mask format using *CleWin* software. A TRE/Electromask Crisscross 251 is used to pattern chrome-on-Pyrex glass masks to less than 2 µm resolution. A 0.4-inch

Table 1
Key specifications and measured performance of the VX 798 Smart-PAD.

Pixel size	130 µm
Pixel thickness	520 µm
Pixel material	Silicon
Number of pixels	48 × 48
Number of timing channels	2
Time gate width (slow mode), FWHM	60 ns
Time gate width (fast mode), FWHM	30 ns
Dead-time	<153 ns
Number of energy channels	2
Energy resolution (slow mode), FWHM	661 eV @ 8 keV

reticle size allows easy patterning of 56 sensors per wafer, as shown in Fig. 1. Four masks are necessary: alignment key, p+ implants, oxide cut, and metallization in preparation for bump-bonding. Diode fabrication steps are as follows:

(i) Etch the alignment key marks. The wafer is cleaned chemically in an oxygen plasma, then reactive ion etched with SF_6. This creates a visible groove a micrometer deep.

(ii) Deposit dry silicon dioxide to a typical thickness of 2630 Å. This is done in a furnace tube dedicated solely to this purpose to avoid contamination which would otherwise lead to higher diode leakage current and sensor noise.

(iii) Front-side (towards electronics) p+ diffusion. We believe doping *via* thermal diffusion as opposed to ion implantation scavenges metal impurities again improving diode performance. For the pixels, BBr_3 is diffused through 60 µm square gaps etched in the SiO_2 and thermally driven in to a depth of approximately 4 µm. Thus the diffusion is about 70 µm wide on a 130 µm spacing. Seven floating guard rings surrounding the array 5 µm wide and 40 µm apart are created at the same time. The estimated p+ doping is $1–10 \times 10^{19}$ cm^{-3}. We then strip the oxide and boron *via* hydrofluoric acid etch and grow new dry oxide to a thickness of 3400 Å.

Figure 1
Photograph of an initial four-inch silicon wafer containing multiple copies of the PAD's sensor interspersed with test structures. Later wafers were patterned with sensors only, varying characteristics such as implant size inside a pixel and the metallization in preparation for commercial bump-bonding. Sensor fabrication was carried out inside our 8000 square-foot class 100 clean room facility (MRDL at NIU).

research papers

(iv) Create the n+ back-side (towards X-ray source) pinning contact. We strip back-side oxide and clean the wafers. $POCl_3$ gas is diffused and driven in, creating doping close to saturation concentrations.

(v) Contact patterning using the oxide cut mask to selectively etch, opening a hole on each pixel slightly smaller than the p+ diffusion.

(vi) Plasma deposition of aluminium metal for the back-side contact.

(vii) Optional aluminium anneal (using H_2 forming gas).

(viii) A series of front-side metallization steps in preparation for stud-bump bonding. The e-beam evaporated metallization used for this program is a Ti/Pd/Au three-layer film with a total stack thickness of 1.2 µm. The metal stack was chosen for its ability to be both soldered to and wire-bonded. The film is patterned using a lift-off technique using image reversal photoresist AZ Electronic Materials 5214.

After processing we verified that the sensors responded to visible light and had low leakage current. During selective sampling of dozens of pixels we typically encountered no bad pixels, giving confidence in our fabrication yield. The stopping power of the 520 µm silicon sensor is close to 100% for low X-ray energies but drops to 50% at 18.3 keV, setting an upper limit to the energy of X-rays which can be efficiently counted. The lower X-ray energy limit is around 2 keV as set by the oxide thickness and the noise of the system as discussed in §3.2.

2.2. Readout ASIC

Each incident X-ray arriving during a 100 ps-wide APS storage-ring bunch creates 0.27 electrons eV^{-1} of deposited energy. From single-diode measurements, with the detector biased with >100 V, we estimate a current pulse width of less than 20 ns. The Voxtel VX-798 ASIC is configured with a 48 × 48 array of mixed signal processing electronics and digital logic for control and readout, fabricated using Taiwan Semiconductor Manufacturing Corp. 0.25 µm CMOS integrated circuit process. A test pixel was placed on the corner of the array having multiple nodes multiplexed to an external test point. The readout operation uses a fully addressable vertical and horizontal scanner, which allows for full frame readout with rates of 135 frames s^{-1} or faster for arbitrary selected pixel readout. This frame rate is not a limitation for pump–probe experiments where integration times of 100 ms or more are typically required, and the dead-time is determined by the synchrotron fill pattern as described in §4.4. Each pixel includes a low-noise front-end amplification circuit followed by two high-gain comparator stages and a digital counter (as seen in Fig. 2). The low-noise front-end uses a capacitive transimpedance amplifier (CTIA) followed by a C-RC shaper circuit. This low-pass/high-pass design has the advantage of lowering noise while maintaining the required temporal

Table 2
Different digital logic modes were designed to make use of the analog circuitry's ability to window the energy of the X-ray (below E_{hi}, above E_{lo}), and its ability to select pulses separated by one bunch time (either 153 ns or 11.4 ns).

B_1 and B_2 indicate bunch times.

Mode	Thresholds	Counter size	Counting mode	Counter 1 data	Counter 2 data
1	Single	30 bit	Continuous	$E_{lo} < E$	–
2	Single	30 bit	Gated	$E_{\neg lo} < E @ B_1$	–
3	Single	2 × 15 bit	Gated	$E_{lo} < E @ B_1$	$E_{lo} < E @ B_2$
4	Dual	30 bit	Continuous	$E_{lo} < E < E_{hi}$	–
5	Dual	30 bit	Gated	$E_{lo} < E < E_{hi} @ B_1$	–
6	Dual	2 × 15 bit	Continuous	$E_{lo} < E$	$E_{hi} < E$
7	Dual	2 × 15 bit	Gated	$E_{lo} < E @ B_1$	$E_{hi} < E @ B_1$
8	Dual	2 × 15 bit	Gated	$E_{lo} < E < E_{hi} @ B_1$	$E_{hi} < E @ B_1$

resolution (Spieler, 2005; Grybos et al., 2005; Brönnimann et al., 2001). Capacitive coupled charge injection circuitry is added to the input of each pixel for calibration purposes. The readout circuit shown schematically in Fig. 2 was specifically designed for APS timing modes and laser pump/X-ray probe applications. By changing passive elements in the shaper such as R_{SHAPER}, C_2 and C_L, the width and amplitude of the pulse can be controlled. The data presented in this paper were taken using a shaping time of about 100 ns, optimized for the standard 24-bunch operating mode of the APS with 153 ns bunch spacing. The detector has also been run with shaping times below 10 ns, suitable for the APS standard 324-bunch mode with 11.4 ns spacing. The thickness of the detector material, and subsequent current pulse width, limits the usefulness of this fast operational mode. The amplified signal is split and fed to two separately controlled comparators (high and low) allowing eight different modes of operation as shown in Table 2. The outputs of the two comparators are gated by external logic signals and sent to two independent 15-bit digital counters. Thus we are able to interleave data collected before and after a sample is excited by a pump pulse (e.g. a femtosecond laser), separated by as little as the X-ray bunch separation time (153 ns). R_{INT} is implemented from drain to
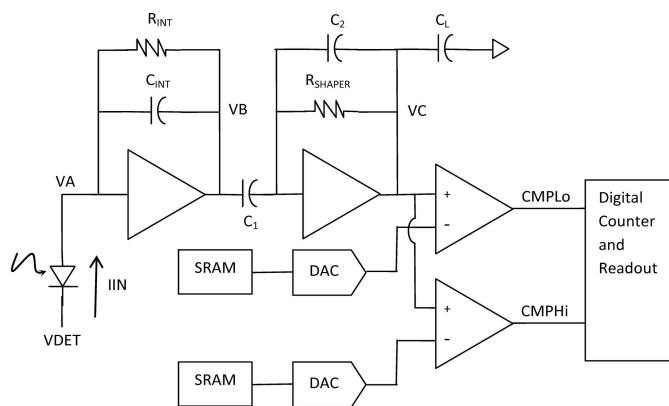

Figure 2
Block diagram of the ASIC electronics associated with each pixel. Low-noise CMOS electronics provide a means to window an energy of interest and count photons into either of two digital counters. The thresholds of the 'low'and 'high' comparators (CMPLo, CMPHi) can be individually calibrated by data latched into a 3-bit static memory (SRAM) and applied by the digital-to-analog converters (DAC).

source of a MOSFET. Its resistance will drop slightly with increasing detector current. The layout of the CMOS circuitry for each pixel is shown in Fig. 3.

2.3. Bump-bonding and packaging

The VX-798 readout integrated circuit (ROIC) was hybridized to the thick photodetector arrays using a stud bump-bonding technique. This technique was selected for the prototype device as the ROIC devices were available only in die form, making traditional indium solder bump hybridization difficult. In the stud bump hybridization technique a small gold bump is placed on each pixel of the ROIC using an automated wire-bond machine. The gold bumps are then coined, dipped in nanosilver paste, and flip-chip hybridized to the matching gold pads of the sensor arrays.

2.4. FPGA readout electronics

Printed circuit electronics derive clocks and provide control of the PAD. We split this functionality into two sets of circuit boards. First we create the bias voltages and currents required by the ASIC on the sensor-ASIC board. To this circuit board we connect VME circuit cards which create the gate signals for the two ASIC counters, high voltage bias for the sensor, supply power, and read image data over Ethernet. The VME electronics derive clocking from the synchrotron's distributed timing (Kline & Ross, 2010).
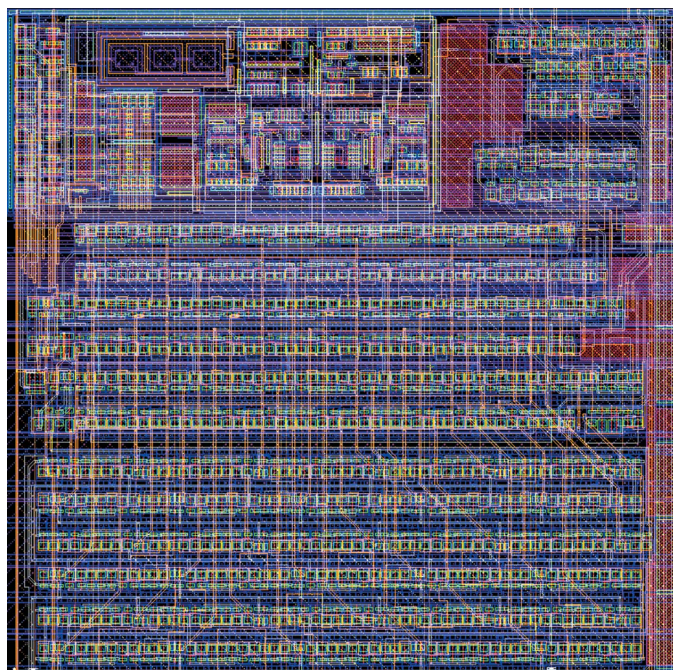

Figure 3
Photoplot of the Silvaco EXPERT computer aided layout of the CMOS circuitry for one pixel. The analog, digital overhead, digital counter and storage registers use 18%, 12%, 40% and 30%, respectively, of the total pixel area. The ASIC was made using the TSMC 0.25 CMOS process.

3. Electrical tests

3.1. Non-uniformity correction

During manufacturing, unavoidable process variations across the integrated circuit result in transistor and passive component mismatch, so that different pixels will have different conversion gains and comparator offsets. If not compensated for, the mismatch in comparator offsets will cause variability across the array in terms of photon detection threshold levels, detection probabilities, and the frequency of false detection events. Calibration in the VX-798 ROIC is performed using two (one for each comparator) 3-bit non-uniformity correction (NUC) blocks. During calibration an electrical signal is injected into a single pixel as the comparator threshold is swept. The inflection point of the S-shaped curve is recorded and the measurement is then repeated for the next pixel in the array. This continues until the discriminator threshold for all 2304 pixels has been determined. A histogram of the pre-NUC discriminator threshold across the VX-798 sensor is shown in Fig. 4. Following characterization of the pre-NUC threshold variation, the data from this measurement can be read back into the sensor in order to individually correct the threshold variation in each pixel using the 3-bit NUC. After applying this correction to the array the threshold non-uniformity was again characterized and found to have a variation of 1.69 mV RMS, *i.e.* 196 eV RMS, 462 eV FWHM. We will use this same S-curve methodology below to determine the electronic noise of the detector from the slope of the curve around the inflection point. Furthermore, the slope of the low-threshold region of the S-curve will be used to determine the charge diffusion depth.

3.2. Leakage current and electronic noise

We measured the reverse bias leakage current of the sensor for individual pixels, test structures of different areas, and for the full PAD. The per-pixel and test structure measurements were made during sensor fabrication and before dicing from the wafer with no guard rings in place. We applied the variable
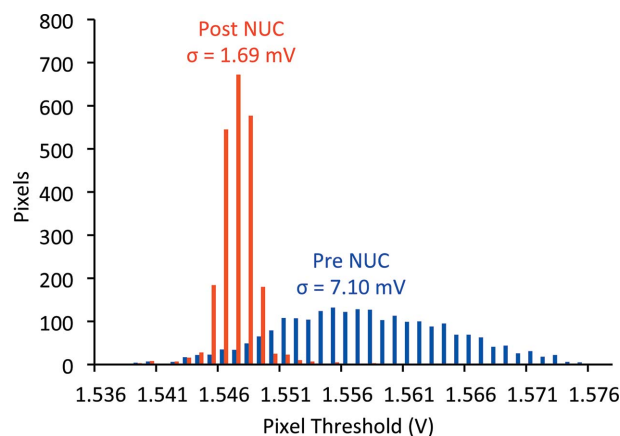

Figure 4
Discriminator threshold variation across the VX-798 sensor pre- and post-threshold correction. Using the 3-bit non-uniformity correction the threshold variation is reduced.

bias voltage to the back side of the wafer at room temperature with a Keithley 4200 probe station and collected current from a single photodiode p+ contact at a time, while leaving the others floating. This current–voltage measurement shown in Fig. 5 probably overestimates the leakage current that is collected when all diodes are connected to ASIC electronics. We noted a small edge effect: the leakage current of pixels at a sensor's perimeter was about six times higher than at positions in the middle of the array. For sensor test structures, the leakage current per area decreases as the area is made larger. It reduces by half for 1 cm^2 diodes compared with the PAD size pixels. For test structures, leakage current typically drops by a factor of three after hydrogen annealing, and so this procedure was also applied to the final detector elements. For all structures the leakage current follows an exponential scaling law with bias voltage (Janesick, 2001) as shown in Fig. 5. To better understand the sources of readout electronic noise and its sensitivity to design parameters we have used both analytical and numerical SPICE models. Two analytical noise models are presented by Spieler (2005): the more versatile assumes the differentiating and integrating time constants are independent, then further simplifies by equating them. Our differentiating time constant τ_D is 80 ns. Our integration time constant τ_I depends on the value of the feedback resistance of the first amplifier circuit. Because this resistance is thus a slow function of the transistor's drain-source current we compute a typical range of 100–150 ns. The sources of readout electronic noise are the diode's series and parallel resistances (R_s and R_p), the sensor's leakage current (I_d), the input transistors voltage (e_n in V Hz$^{-1/2}$) and current (i_n in A Hz$^{-1/2}$) noises. Using $\tau_I = \tau_D = \tau = 80$ ns, the noise in electrons RMS can be calculated from

$$e_{\text{RMS}} = \frac{1}{q}\left\{0.924\left[\left(2qI_d + \frac{4kT}{R_p} + i_n^2\right)\tau \right.\right.$$
$$\left.\left. + \left(4kTR_s + e_n^2\right)\frac{C_d^2}{\tau} + 4A_fC_d^2\right]^{1/2}\right\} \quad (1)$$

where k is Boltzmann's constant, q is the electron charge, the temperature $T = 300$ K, and A_f is the $1/f$ amplifier noise constant (here set to zero). This equation is plotted in Fig. 6. From the forward-bias portion of a single sensor-diode current–voltage curve we estimate that $R_s < 1000$ Ω. From the reverse-bias portion we estimate $R_p > 10^9$ Ω (*i.e.* the derivative of voltage with respect to current in Fig. 5 multiplied by 48×48). Spieler's analytical models combine all circuit input capacitance into a single value, which we estimate to be the approximate sum of the diode capacitance, the sensor fringing capacitance pixel-to-pixel and any input capacitance of the stud-bump-bonded ASIC, approximately 3 fF, 15 fF and 35 fF, respectively. For analytical calculations we use $e_n = 10$ nV Hz$^{-1/2}$ and $i_n = 1$ fA Hz$^{-1/2}$, typical of commercial CMOS amplifiers. Then, to better model the transistor noise we employ SPICE circuit simulations. Around these baseline circuit values, the analytical results show sensitivity mainly to I_d and C_d, less to e_n, i_n and R_s. We observe reasonable
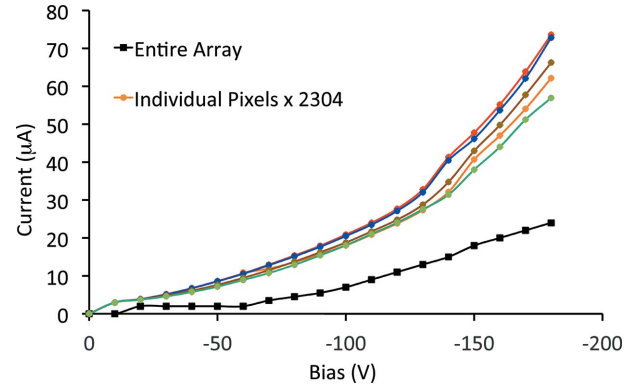

Figure 5
PAD sensor diode leakage current *versus* bias voltage at room temperature. The lower curve was measured by the DC voltage supply to the full PAD array. In comparison, the upper set of five traces were measured for different individual pixels at the un-diced wafer level and then scaled (multiplied) by the number of total pixels. A typical per pixel leakage current is 10 to 20 nA with no evidence of breakdown at high voltage.

agreement between the analytical, SPICE and measured noise values (80 to 100 e_{RMS}, see §4.2). To dramatically alter these results, R_s would have to exceed 10^4 Ω, and R_p would have to drop below 10^7 Ω. Our guidelines for future designs then are to lower I_d while preserving a clean diode fabrication process to maintain otherwise good current–voltage characteristics. For our next, larger, PAD we will bias the guard rings around the array. Such back-side p+ structures both floating and connected to ASIC circuit potential should lower the leakage current generated at the saw-cut of the die, an area of considerable damage to the silicon. Our models would then predict 450 eV FWHM energy resolution at the 40 ns time constants expected for an upgraded Advanced Photon Source storage ring.
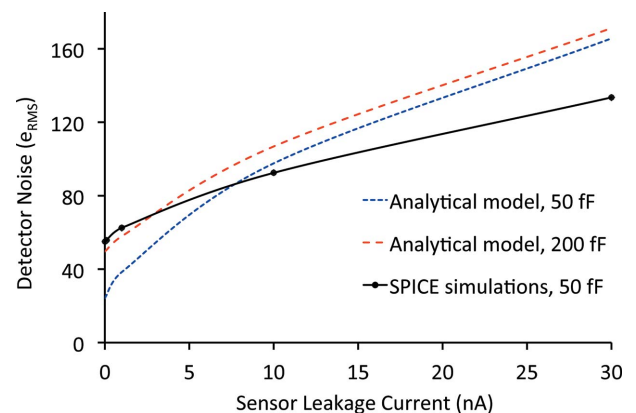

Figure 6
Model for readout electronic noise as a function of sensor leakage current (considered to be one of its main sources) for different values of the diode capacitance, C_d. The model makes use of a number of circuit parameters each measured or estimated by other means. The measured noise value (from the energy resolution measurements discussed below) is 80 to 100 electrons RMS. Hence we infer that we understand the dominant noise sources and have a guide both analytical and from SPICE for future sensor-ROIC improvements.

4. X-ray characterization

X-ray measurements were conducted at beamline 7-ID of the Advanced Photon Source. This facility is dedicated to time-resolved research, particularly pump–probe experiments requiring ultrafast and high-intensity lasers including time-resolved X-ray fluorescence, microscopy, scattering and imaging (Dufresne *et al.*, 2010). A diamond (111) mono-chromator followed by a 200 mm Rh-coated mirror for harmonic rejection delivers beam to the center of a six-circle Huber diffractometer. For these preliminary tests, the detector was mounted 0.7 m behind the diffractometer center on a horizontal translation stage as shown in Fig. 7. Since these tests were conducted, the detector has been repackaged so that it mounts directly onto the diffractometer arm following an optional flight tube.

4.1. Collection efficiency, spatial uniformity and resolution

To map the spatial uniformity of the PAD, we plot the array's response to a flood illumination of 8 keV X-rays, produced by placing several layers of polyimide film at the diffractometer center. We observed that 91% of the pixels linearly respond to X-ray signals, 8% of the pixels had little response (dark pixels), and 1% of the pixels had abnormally high response (hot pixels). Dark pixels tend to cluster on the edges, perhaps indicating inadequate stud bump-bonding there. Future versions of this detector will use an improved higher yield indium bump-bonding process to mitigate this effect.

We characterized the collection efficiency of the pixel array detector by summing the counts from 25 pixels located at the center of the detector for a fixed integration time as a function of reverse-bias voltage, as shown in Fig. 8. We observe a rapid fall-off below about 100 V reverse bias.

We characterized the PAD's imaging quality by quantifying the optical spread in a step in X-ray intensity, the spread from a point source image, and from measurements of charge
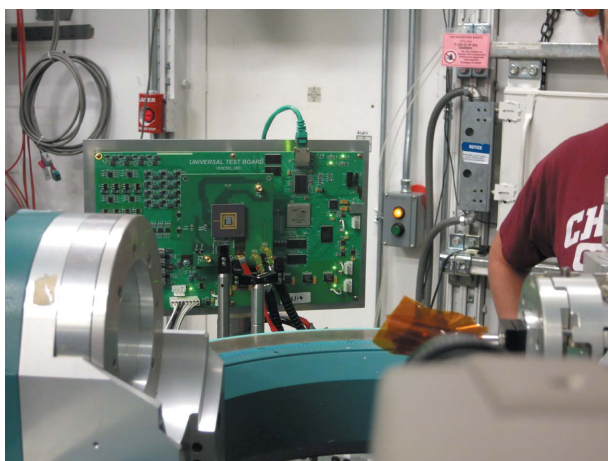

Figure 7
Detector testing configuration behind the diffractometer. A variety of samples, including polyimide film (shown), fluorescence targets and an InSb wafer for diffraction studies, were placed at the diffractometer center. The PAD is centered in the circuit board. We have since packaged the detector in a more flexible electronic enclosure.
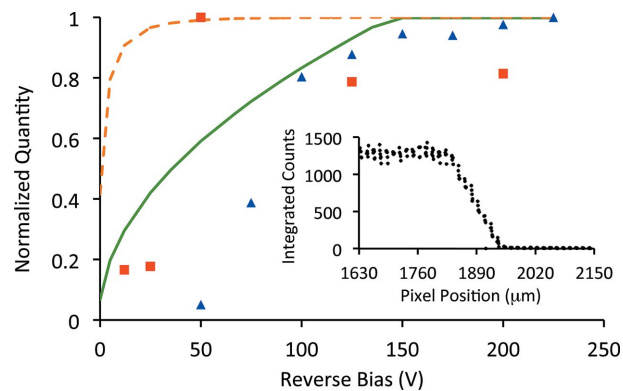

Figure 8
Detector bias voltage optimization. The measured count rate normalized to its maximum (triangles) and relative sharpness of the line spread function (squares) are shown as functions of sensor bias voltage. The inset displays a typical sharpness of the line spread function. The horizontal tick marks on the inset are 130 μm, or 1 pixel. For comparison, these measured parameters are shown alongside the calculated reverse-bias depletion depth normalized to the 520 μm pixel thickness (solid line) and the fraction of 8 keV X-rays absorbed within this depth (dashed line). The simple assumption that X-rays are only absorbed in the diode depletion region does not fully account for the count rate *versus* bias data, but is a contributing consideration.

diffusion derived from S-curve measurements. We also placed a knife-edge absorber very close to the sensor at a slight angle to the pixel grid under conditions of uniform X-ray illumination. Following published methodologies we merge data from all columns in the image to generate an overall profile of counts *versus* distance along an image row allowing spatial interpolation smaller than the pixel size (Buhr *et al.*, 2003; Estribeau & Magnan, 2004). Comparing the slope of such profiles taken at different bias levels we quantify increased blurring below 50 V bias: the knife edge appeared more gradual, its slope less.

We measured blurring of an optical point source created by placing a 50 μm-diameter pinhole target near the array. This method provides less information as few pixels are actually sampled; we observed sharp images and no significant variation over 50 V to 200 V bias. We also measured S-curves as a function of sensor bias for 7.33 keV X-rays. (These measurements were taken at APS beamline 8-ID.) Recalling the methodology from Kraft *et al.* (2009), we estimate pixel charge sharing measured in micrometers into an adjoining pixel. We see a dramatic increase indicating blurring at sensor voltages below about 100 V (Fig. 9). Considerations of optimum sensor bias for counting efficiency and minimal blurring help set operating parameters (*e.g.* maintaining the bias voltage above 125 V) and also impact decisions for any follow-on sensor which might be thicker to improve our hard X-ray collection efficiency. For an incoming X-ray photon to make a digital count, the photocharge must arrive at the collecting anode without significant reduction from recombination or charge sharing. Depending on the exact n− doping concentration and carrier mobility, a reverse bias voltage of 90 to 150 V will fully deplete the 520 μm-thick lightly doped (mid-10^{11} cm^{-3}) material. As the bias voltage is lowered, the depletion width narrows. If we assume that no photocharge from outside such
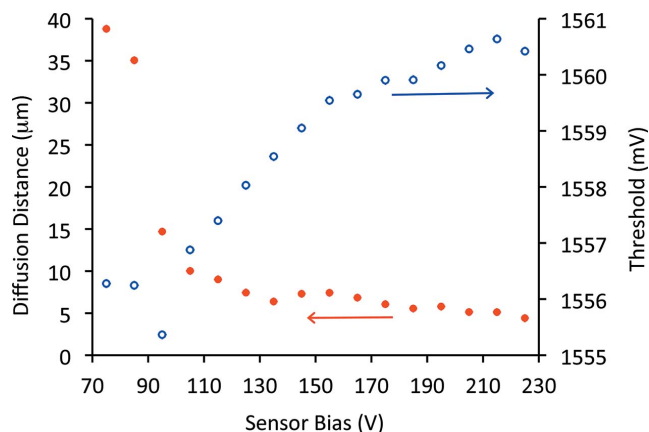
Figure 9
Evidence for interaction between the sensor and ROIC. S-curve data were analyzed for different sensor bias voltages to quantify charge diffusion and threshold shifts. Below 100 V bias, the sensor is not fully depleted and does not perform optimally. Above 100 V there is evidence that the pulse shapes are sharpening as slightly higher thresholds are needed for their detection.

Figure 10
Energy calibration and resolution. Sweeping the energy threshold (millivolts) yields the detector's energy resolution by fitting the derivative of the count rate to a Gaussian curve. We can thus distinguish X-ray fluorescence from neighboring elements and use the peak position to calibrate the detector (inset).

a region is collected, we could model the detector's counting efficiency as a function of bias voltage. We compute the width of the depletion (plotted normalized to the sensor thickness) using standard diode physics, a step diffusion power law either analytically or using a one-dimensional numerical model (Winston & Hayes, 1995). We then compute the X-rays exponentially absorbed in such width assuming a mass normalized absorption of $66.3 \text{ cm}^2 \text{ g}^{-1}$ and density 2.33 g cm^{-3}. These modeled results are shown together with the measured count rate in Fig. 8, and indicate rough agreement. However, other effects also seem to be occurring. Decreasing the photodiode reverse bias decreases the electric field across the PN junction in the photodetector, likely resulting in increased current pulse widths out of the photo-detector into the ASIC. We can model this by finite-element analysis based on Ramo's theorem. The pulse area is set by the input charge, so an increasing width must result in a lowering peak. Circuit simulations of the VX-798 design show that the conversion gain of the pixel electronics begins to drop as the width extends beyond 20 ns. We see experimental evidence of this effect (Fig. 9) by observing how the comparator threshold voltage needed to detect an X-ray shifts to slightly higher values as the sensor bias increases (again using the S-curve *versus* sensor bias data). Higher sensor bias produces higher leakage current, which leads to lower R_{INT} MOSFET resistance, and hence lower amplifier gain. So, as the sensor bias rises, the pulse must sharpen faster than the ROIC gain drops. In the future we will further characterize our sensors looking for even more subtle effects at varying X-ray energies (Cho *et al.*, 1992).

4.2. Energy calibration and resolution using X-ray fluorescence

To calibrate the energy response and resolution of the detector, we removed the polyimide scattering film and replaced it with four d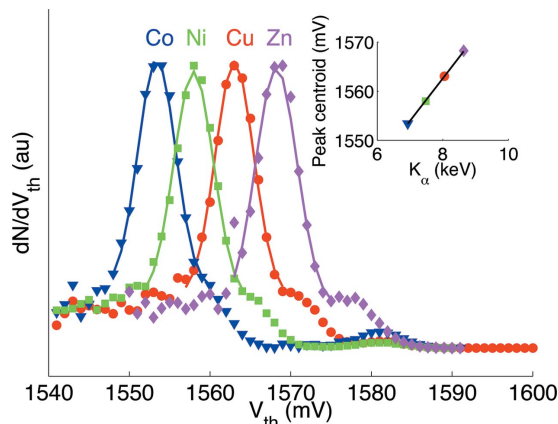ifferent X-ray fluorescence standards in succession: Co, Ni, Cu, Zn (Z = 27, 28, 29, 30). With the incident X-ray beam at 10 keV, an S-curve was recorded for each element. The normalized derivatives for each scan are shown in Fig. 10 and demonstrate distinct peaks for each element. The peak centroids are plotted in Fig. 10 (inset) to give an energy calibration of $8.6 \pm 0.1 \text{ mV keV}^{-1}$ (linearity $R^2 = 0.96$). This compares with the design energy calibration in this X-ray energy range of 11 mV keV^{-1}. The average peak width of the four elements in Fig. 10 is 661 eV FWHM, corresponding to the 80 electrons RMS noise used in Fig. 6. We measure 0.8 to 3.3 μm charge diffusion for 7 to 12 keV X-rays, small compared with the 130 μm pixel.

4.3. Time-resolved X-ray diffraction

If an X-ray detector can be temporally gated to a single bunch it is possible in principle to conduct pump–probe experiments where the time resolution is limited only by the synchrotron X-ray pulse duration of ~100 ps FWHM. In practice, however, it is difficult to measure subtle changes induced by the probe pulse if only one timing gate is available, since any long-term drift in the sample, the X-ray beamline (including top-up effects) or the pump pulse can quickly wash out small time-dependent effects. This has been a major disadvantage of all gated area detectors so far, including detectors that use mechanical choppers to isolate single bunches. The smart-pixel technology, however, allows the 'high' and 'low' channels to be assigned to temporal gates, rather than just energy levels (see Table 2). Typically the gates are assigned to the same X-ray bunch, separated by one storage ring round trip, with the pump pulse (usually a laser pulse) coincident with the late pulse to within a desired time-delay. Using the 5029 Hz amplified femtosecond laser at APS beamline 7-ID as the pump pulse trigger, we scanned the detector gate over subsequent X-ray bunches as shown in Fig. 11. These data clearly reveal the 153 ns pulse structure of the APS storage ring in 24-bunch mode, gated to 10 ns or
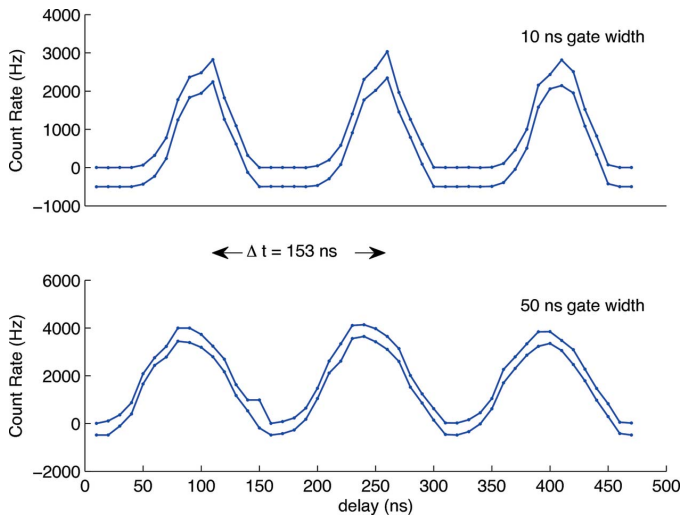
Figure 11
Time resolution. The detector can be gated (here 10 ns or 50 ns widths) to select out single bunches. This allows the system timing resolution to be set by the synchrotron storage ring bunch length, around 100 ps. Each figure shows adjacent revolutions of the same bunch in the storage ring triggered at 5029 Hz and are offset for clarity. The two gates were collected simultaneously with the two different counting channels.

50 ns. The pattern is identical in both the early, or laser 'off', channel and the later, laser 'on', channel.

The standard test sample for time-resolved X-ray diffraction (TRXD) is fast modulation of the (004) diffraction peak of an indium antimonide (InSb) wafer following intense ultrafast laser excitation at 800 nm (Chin *et al.*, 1999). To duplicate these measurements, we aligned a (100) cut, 0.5 mm-thick polished InSb wafer to the 10 keV beam at the diffractometer center. Diffracting in the horizontal plane, we were able to translate the detector into the (004) diffraction spot. One second exposures of the 'off' and 'on' channels were recorded simultaneously and are shown at the top of Fig. 12. At a fluence of ~ 1 mJ cm^{-2}, the laser causes the peak to shift to lower angles (implying larger d-spacings), decrease in intensity and increase in width.

Careful measurement of these line-shapes at different delay may be used in conjunction with dynamical diffraction theory to explore the interplay of heat, sound, electrical and optical transport at picosecond timescales inside semiconductors. Here we simply analyzed the total counts in the laser 'on' and 'off' timing channels in the lower portion of Fig. 12. When the laser strikes the sample before the 'on' X-ray gate, the detector records no significant difference between the static, or laser 'off', gate. The peak intensity suddenly drops within the X-ray bunch duration of 100 ps as the laser pulse delay is swept over the 'on' bunch at a delay of 0 ns. The total intensity eventually recovers with a double-exponential dependence to the static state before the next laser pulse. Curve-fitting the decay yields characteristic times of $\tau_1 = 0.8$ ns and $\tau_2 = 100$ ns. Associating these time constants with the acoustic and thermal properties of the material, respectively, and assuming that they persist for twice the X-ray probe (extinction) ($\zeta = 1.239$ μm at 10 keV) depth allows us to calculate the speed of sound v_{sound} and one-dimensional thermal diffusivity $D_{thermal}$ for InSb,
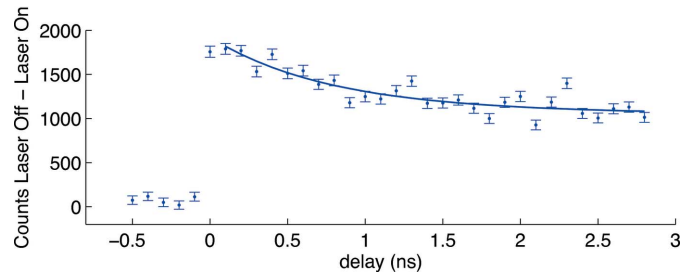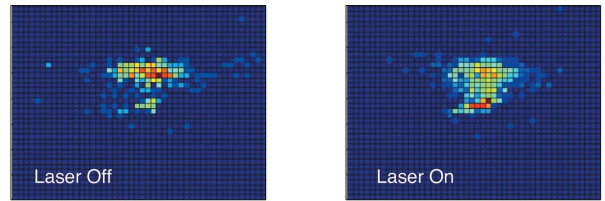

Figure 12
Time-resolved X-ray diffraction from ultrafast laser-excited InSb. The two images are separated by 100 ps. The diffraction angle increases in the vertical direction, and this line shape could be analyzed to determine the depth-dependent strain profile. Here a simpler analysis is carried out by calculating the count rate difference as a function of laser/X-ray delay times (lower figure). Errors are estimated from the isolated dead-time model. Fitting the transient behavior to a double exponential (solid line) yields time constants of 0.8 ns and 100 ns, which may be used to estimate the longitudinal acoustic velocity and thermal diffusion speed of InSb.

$$v_{sound} = 2\zeta/\tau_1 = 3098 \text{ m s}^{-1} \qquad (2)$$

and

$$D_{thermal} = (2\zeta)^2/4\tau_2 = 0.15 \text{ cm}^2 \text{ s}^{-1}. \qquad (3)$$

These compare with tabulated values of $v_{sound} = 3400$ m s^{-1} for longitudinal sound waves along the (001) direction and $D_{thermal} = 0.16$ cm^2 s^{-1}.

4.4. Linearity

A linearity test was performed to show that the dead-time of the detector is determined by the synchrotron X-ray source repetition rate, and not by the detector itself. The diffraction sample was removed and the detector was placed into direct beam. The incident intensity was adjusted over several orders of magnitude using remotely operated attenuation filters, and monitored using an ionization chamber. In TRXD experiments, detectors are typically temporally gated as described above and are often operated far into their nonlinear response regime to compensate for the low repetition rate of the pump pulse. Therefore we also conducted our linearity measurement in temporal gating mode, again synchronized to the laser repetition rate of 5029 Hz. Choosing the brightest pixel in the center of the X-ray beam, we found it responded linearly to the incident rate up to approximately 1000 Hz. Above this count rate, the detector response was sub-linear as seen in Fig. 13. Ideally each element of the detector should have a response identical to a fast-counting avalanche photodiode, corresponding to the isolated dead-time model (Walko *et al.*, 2008),
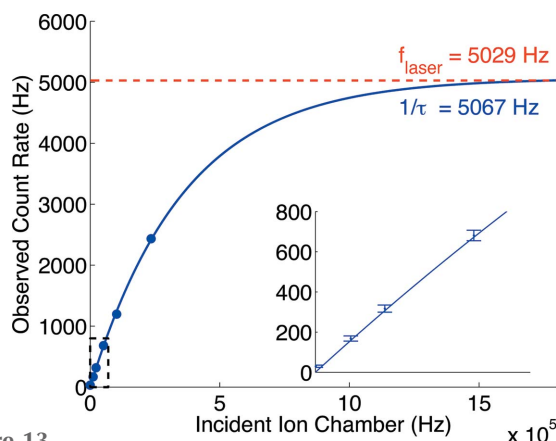
Figure 13
Detector linearity. The detector response at low cout rates is linear (inset) and fits an isolated dead-time model (solid line) at higher rates which extrapolates approximately to the gated X-ray repetition rate of 5029 Hz (dashed line).

$$N_{\mathrm{T}} = -\frac{1}{\tau} \ln(1 - N_0 \tau), \qquad (4)$$

where N_0 is the observed count rate, N_{T} is the true, or incident, count rate, and τ is the spacing between pulses which is equivalent to the isolated dead-time. Curve-fitting to this model yielded a dead-time of $1/\tau = 5067$ Hz, in agreement with the laser repetition rate of 5029 Hz. Extrapolating to the entire pixel array and ungated operation, this indicates the detector would be capable of an optimal count rate (Walko *et al.*, 2010) of $(48 \times 48 \text{ pixels})/(3 \times 153 \text{ ns})$, or nearly 5 GHz in the APS 24-bunch mode.

5. Conclusion and outlook

The development of this smart-pixel technology was originally motivated by the desire to record multiple energy and timing channels from an area detector. The demand for this capability has been particularly strong from the time-resolved X-ray science community, which has been limited either to single-element detectors or to recording data without normalization. We therefore anticipate that this smart-pixel technology will be rapidly adopted by most time-resolved researchers presently using single-element counting detectors. For example, APS 7-ID has been dedicated to time-resolved research for over a decade, and nearly half of the time-resolved publications from this beamline have exclusively used single-element detectors for data acquisition. These experiments may obtain order-of-magnitude improvements in data collection time by adopting this area detector, where each pixel has the capabilities of previous single-element detectors (*e.g.* avalanche photodiodes). The ability to optimize in software the energy resolution, time resolution and digital logic mode should allow customization of the detector to each experiment, as well as adapting the performance for different storage ring fill patterns. We also anticipate that this detector may be adopted by some time-resolved X-ray experiments presently using either single-gate area detectors or mechanically chopped X-ray beams with conventional area detectors.

These experiments now are limited to only investigating relatively large time-resolved effects (1% or more) due to experimental drift. The adoption of a multiple-channel detector for collecting normalized data should help the signal-to-noise ratio of these experiments to approach the fundamental counting statistics limit, as nearly achieved now in many other synchrotron radiation techniques.

Several other unanticipated applications of the smart-pixel detector have recently emerged. One of these is non-thermal diffuse scattering, where non-equilibrium phonon populations are produced using ultrafast laser excitation. To date these experiments have been limited to regions of reciprocal space far away from Bragg peaks, where the backgrounds are small (Trigo *et al.*, 2008). Following these short-lifetime excitations as they decay into lower wavevector acoustic phonons closer to Bragg peaks is important for understanding nanoscale thermal transport; this detector should make it possible to simultaneously measure scattering from thermal *versus* non-thermal phonons throughout the entire Brillouin zone. Another unanticipated development has been found with the storage-ring multi-bend achromatic lattice, which may allow upgraded storage rings to improve their spatial coherence by several orders of magnitude. This in turn makes possible X-ray photon correlation spectroscopy at nanosecond timescales. Using the conventional fast-framing detector approach, this would imply that nearly GHz frame rate detectors would be necessary to match the improved beam brightness. Recent work with double-pulsed laser beams in dynamic light scattering (Lee *et al.*, 2014) has shown that as an alternative approach it is possible to experimentally determine correlation coefficients using time gating, rather than fast framing. A similar approach should be possible with this detector, which could be optimized at the expense of energy resolution to discriminate bunches close to a synchrotron's maximum fill pattern of a few nanoseconds bunch separation.

References

Adams, B. W., Mane, A. U., Elam, J. W., Obaid, R., Wetstein, M. & Chollet, M. (2015). *J. Synchrotron Rad.* **22**, 1202–1206.
Brönnimann, Ch., Baur, R., Eikenberry, E., Kohout, S., Lindner, M., Schmitt, B. & Horisberger, R. (2001). *Nucl. Instrum. Methods Phys. Res. A*, **465**, 235–239.
Buhr, E., Günther-Kohfahl, S. & Neitzel, U. (2003). *Medical Imaging 2003*, pp. 877–884. International Society for Optics and Photonics.
Campbell, M., Heijne, E., Meddeler, G., Pernigotti, E. & Snoeys, W. (1998). *IEEE Trans. Nucl. Sci.* **45**, 751–753.

Chin, A., Schoenlein, R., Glover, T., Balling, P., Leemans, W. & Shank, C. (1999). *Phys. Rev. Lett.* **83**, 336–339.

Cho, T., Takahashi, E., Hirata, M., Yamaguchi, N., Teraji, T., Matsuda, K., Takeuchi, A., Kohagura, J., Yatsu, K., Tamano, T., Kondoh, T., Aoki, S., Zhang, X. W., Maezawa, H. & Miyoshi, S. (1992). *Phys. Rev. A*, **46**, R3024–R3027.

Dufresne, E. M., Adams, B., Arms, D. A., Chollet, M., Landahl, E. C., Li, Y. & Walko, D. A. (2010). *AIP Conf. Proc.* **1234**, 181–184.

Ejdrup, T., Lemke, H. T., Haldrup, K., Nielsen, T. N., Arms, D. A., Walko, D. A., Miceli, A., Landahl, E. C., Dufresne, E. M. & Nielsen, M. M. (2009). *J. Synchrotron Rad.* **16**, 387–390.

Estribeau, M. & Magnan, P. (2004). *Optical Systems Design*, pp. 243–252. International Society for Optics and Photonics.

Grybos, P., Rodriguez, A. C., Idzik, M., Gaitan, J. L., Prino, F., Ramello, L., Swientek, K. & Wiacek, P. (2005). *IEEE Trans. Nucl. Sci.* **52**, 839–846.

Henrich, B., Bergamaschi, A., Broennimann, C., Dinapoli, R., Eikenberry, E., Johnson, I., Kobas, M., Kraft, P., Mozzanica, A. & Schmitt, B. (2009). *Nucl. Instrum. Methods Phys. Res. A*, **607**, 247–249.

Janesick, J. R. (2001). *Scientific Charge-Coupled Devices*, Vol. 117. Bellingham: SPIE Press.

Kline, D. M. & Ross, S. K. (2010). *Proceedings of the 8th International Workshop on Personal Computers and Particle Accelerators (PCaPAC)*, 5–8 October 2010, Saskatoon, Canada.

Koerner, L. J. & Gruner, S. M. (2011). *J. Synchrotron Rad.* **18**, 157–164.

Kraft, P., Bergamaschi, A., Broennimann, Ch., Dinapoli, R., Eikenberry, E. F., Henrich, B., Johnson, I., Mozzanica, A., Schlepütz, C. M., Willmott, P. R. & Schmitt, B. (2009). *J. Synchrotron Rad.* **16**, 368–375.

Lee, S., Jo, W., Wi, H. S., Gutt, C. & Lee, G. W. (2014). *Opt. Express*, **22**, 21567–21576.

Nüske, R., van Korff Schmising, C., Jurgilaitis, A., Enquist, H., Navirian, H., Sondhauss, P. & Larsson, J. (2010). *Rev. Sci. Instrum.* **81**, 013106.

Ross, S., Haji-Sheikh, M. & Westberg, G. (2013). *Instrumentation and Measurement Technology Conference (I2MTC), 2013 IEEE International*, pp. 1017–1021. IEEE.

Rossi, G., Renzi, M., Eikenberry, E. F., Tate, M. W., Bilderback, D., Fontes, E., Wixted, R., Barna, S. & Gruner, S. M. (1999). *J. Synchrotron Rad.* **6**, 1096–1105.

Spieler, H. (2005). *Semiconductor Detector Systems*. Oxford University Press.

Trigo, M., Sheu, Y., Arms, D., Chen, J., Ghimire, S., Goldman, R., Landahl, E., Merlin, R., Peterson, E., Reason, M. & Reis, D. A. (2008). *Phys. Rev. Lett.* **101**, 025505.

Vernon, W., Allin, M., Hamlin, R., Hontz, T., Nguyen, D., Augustine, F., Gruner, S., Xuong, N. H., Schuette, D., Tate, M. & Koerner, L. (2007). *Proc. SPIE*, **6706**, 67060U.

Walko, D. A., Arms, D. A., Dufresne, E. & Landahl, E. C. (2010). *AIP Conf. Proc.* **1234**, 856–859.

Walko, D. A., Arms, D. A. & Landahl, E. C. (2008). *J. Synchrotron Rad.* **15**, 612–617.

Williams, G. M., Rhee, J., Zou, H., Lee, A. & Ross, S. (2013). In *Nuclear Science Symposium and Medical Imaging Conference (NSS/MIC)*, pp. 1–9. IEEE.

Winston, D. & Hayes, R. (1995). *Compound Semiconductors*, *Institute of Physics Conference Series*, Vol. 141, pp. 747–750.